Studies of Sea-Ice Thickness and Salinity Retrieval Using 0.5–2 GHz Microwave Radiometry

Oguz Demir, Joel T. Johnson, *Fellow, IEEE*, Kenneth C. Jezek, Marco Brogioni, *Member, IEEE*, Giovanni Macelloni, *Senior Member, IEEE*, Lars Kaleschke, and Ludovic Brucker

***Abstract*— Arctic sea-ice thickness and salinity retrievals are simulated to explore the performance of nadir-observing microwave radiometry operating with up to 16 frequency channels in the 0.5–2-GHz frequency range. A radiative transfer model is used to create lookup tables of the circularly polarized thermal emissions of first-year (FY) and multiyear (MY) sea ice, and the performance of two distinct retrieval methods is examined. The first method retrieves only sea-ice thicknesses, while the second retrieves both ice thickness and ice salinity. Retrieval errors are simulated for both FY and MY sea ice as a function of ice thickness, salinity, and temperature to investigate the impact of radiometric uncertainty, the frequency channels used, and any errors in ancillary information. To gain further insight into Arctic scale retrieval performance, a simulated brightness temperature dataset is produced for Arctic sea ice for the period October 2020–March 2021 using sea-ice thicknesses from the SMOS-CryoSat-2 algorithm. Compared to existing sea-ice thickness retrievals obtained from 1.4-GHz microwave radiometers, the results demonstrate that 0.5–2-GHz radiometry can achieve higher sensitivity to a sea-ice thickness within the range 0.5–1.5 m for FY sea ice and enable the retrieval of multiple sea-ice parameters (thickness and salinity) simultaneously.**

***Index Terms*— Microwave radiometry, radiative transfer, remote sensing, sea ice.**

I. Introduction

ARCTIC sea ice is a crucial element of the Earth's cryosphere that impacts the global climate system by regulating energy transfers between the ocean and atmosphere, reflecting incoming solar radiation, influencing salt and freshwater fluxes through melt/freeze cycles and circulation, and circulating biological and chemical components. The rapid reduction in sea-ice extent and thickness observed in the Arctic in recent decades [1], [2] motivates the development of novel remote sensing approaches to quantify changes for both thin and thick ice.

Microwave radiometry has been used to estimate ice concentration and extent for decades [3], [4], and sea-ice motion has been sensed using both active and passive microwave instruments [5]–[7]. Ice thicknesses up to 0.5 m can be estimated using infrared and optical observations combined with thermodynamic models [8]–[11] but require cloud-free observations. Radar altimeters, such as CryoSat-2, and laser altimeters, such as Ice, Cloud, and land Elevation Satellite (ICESat-2), have been shown capable of retrieving ice thicknesses from freeboard measurements [12], [13]; however, the obtained thickness estimates experience greater relative uncertainties for ice thicknesses below approximately 1 m. Microwave radiometers operating at 1.4 GHz ("L-band"), such as SMOS and Soil Moisture Active Passive (SMAP), can also retrieve sea-ice thickness [14]–[17] but experience increased retrieval errors as ice thicknesses exceed 0.5 m for closed sea ice due to the limited penetration depth at 1.4 GHz. The combined use of CryoSat-2 and SMOS observations has been shown to overcome the limitations of the individual sensors [18], but retrieval errors remain at least ∼30% for ice thicknesses in the 0.5–1.2-m range. The use of microwave radiometry at frequencies less than 1.4 GHz can extend performance to ice of greater thickness [19]. However, potential human-made radio frequency interference (RFI) at these frequencies due to their allocation and the requirement for a large antenna size has, to date, discouraged the use of space-borne microwave radiometry at frequencies of less than 1.4 GHz.

Recently, the airborne and ground-based Arctic campaigns of the ultrawideband software-defined microwave radiometer (UWBRAD) [20]–[22] have demonstrated brightness temperature (TB) measurements from 0.5 to 2 GHz in the presence of the small to moderate RFI of Earth's polar regions. The instrument operates in 12 frequency channels (each of ∼88-MHz bandwidth) from 0.5 to 2 GHz, obtains a radiometric uncertainty of ∼1 K per channel, and applies advanced RFI detection and mitigation algorithms to filter RFI contributions [23], [24]. These results motivate further examination of the potential of 0.5–2-GHz microwave radiometry for remotely sensing sea-ice thickness.

Beyond the retrieval of sea-ice thickness, the retrieval of sea-ice salinity is also of interest. The salinity of sea ice

Manuscript received November 24, 2021; revised March 6, 2022; accepted April 3, 2022. Date of publication April 18, 2022; date of current version May 4, 2022. *(Corresponding author: Oguz Demir.)*

Oguz Demir and Joel T. Johnson are with the Electroscience Laboratory, The Ohio State University, Columbus, OH 43210 USA (e-mail: demir.15@buckeyemail.osu.edu; johnson.1374@osu.edu).

Kenneth C. Jezek is with the Byrd Polar and Climate Research Center, The Ohio State University, Columbus, OH 43210 USA (e-mail: jezek51@gmail.com).

Marco Brogioni and Giovanni Macelloni are with the Institute for Applied Physics, 50019 Florence, Italy (e-mail: m.brogioni@ifac.cnr.it; g.macelloni@ifac.cnr.it).

Lars Kaleschke is with the Alfred-Wegener-Institut Helmholtz-Zentrum für Polar und Meeresforschung, 27570 Bremerhaven, Germany (e-mail: lars.kaleschke@awi.de).

Ludovic Brucker is with the Center for Satellite Applications and Research, National Oceanic and Atmospheric Administration (NOAA)/NESDIS, College Park, MD 20740 USA, and also with the U.S. National Ice Center, Suitland, MD 20746 USA (e-mail: ludovic.brucker@noaa.gov).

Digital Object Identifier 10.1109/TGRS.2022.3168646

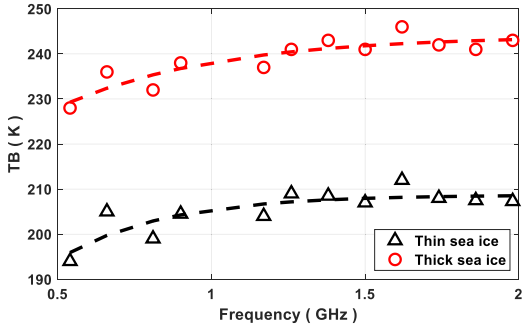

Fig. 1. Sample airborne UWBRAD TB spectra measured over thin and thick sea ice in the Lincoln Sea, northern Greenland in September 2017 [28]. Markers indicate the measured TB in 12 frequency channels, while dashed lines represent the corresponding exponential fits.

affects its thermal and dielectric properties and ice–ocean salt and freshwater exchanges. Outflows of freshwater from melting sea ice and sea salinification during sea-ice formation are key processes that dominate freshwater budgets and their variability in the polar oceans [25]. Higher salinity dense water is produced particularly on the Arctic and Antarctic continental shelves where polynyas allow continuous sea-ice growth [26]. Sea-ice salinity is yet to be determined from satellite measurements; current information is derived only from sparse *in situ* datasets or from models [27]. In [28], it was demonstrated that multifrequency measurements from an airborne radiometer (see example in Fig. 1) have the potential to allow simultaneous retrieval of both ice thickness and salinity.

This article reports a theoretical study that explores the capabilities of 0.5–2-GHz microwave radiometry for the retrieval of sea-ice properties. The study applies a radiative transfer model to simulate sea-ice thermal emission in the 0.5–2-GHz band, and a multichannel retrieval algorithm is introduced to retrieve sea-ice thickness and/or salinity from simulated TB observations. The impacts of radiometric uncertainty and errors in ancillary information on retrieval performance are investigated for both first-year (FY) and multiyear (MY) sea-ice types. Retrieval performance is examined for a thickness-only (TO) retrieval (in which ancillary ice salinity information is assumed available) and a thickness-salinity (TS) retrieval in which both parameters are estimated simultaneously. The impact of the particular set of frequency channels used is also investigated. Further simulations of both the TO and TS retrieval approaches are then reported to examine average retrieval performance over the Arctic for the period October 2020–March 2021.

Section II summarizes the sea-ice emission model, while Section III describes the retrieval algorithms proposed and reports the results obtained for fixed sea-ice conditions. Section IV describes average retrieval performance in the Arctic-scale simulation. Finally, Section V provides concluding remarks.

II. Sea-Ice Emission Model

Sea ice is described in this work as a planar layered medium consisting of sea ice and snow layers bounded by semi-infinite air and ocean media. The ice and snow layers are then described by their thickness and relative permittivity.

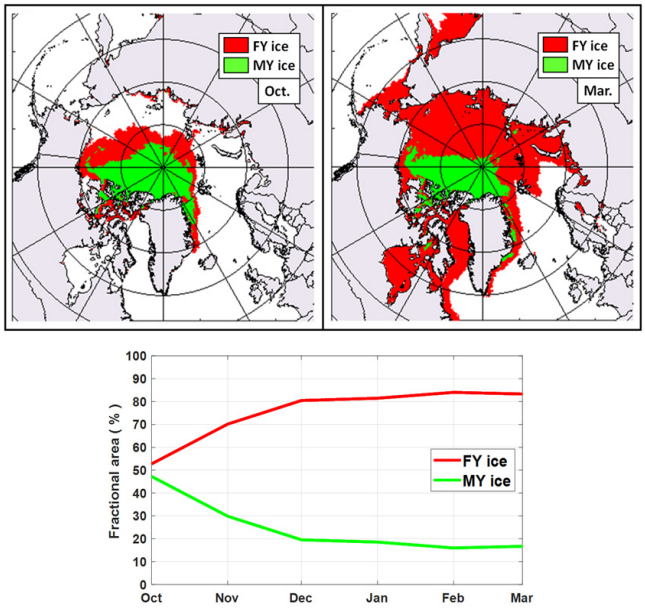

Fig. 2. FY (red) and MY (green) ice distributions in the Arctic in October 2020 (top left) and March 2021 (top right) [29]. The fractional sea-ice coverage in each ice type during this period is also shown (bottom).

A. Sea Ice, Snow, and Sea Water Permittivities

Sea-ice dielectric properties are greatly affected by the saline brine volume fraction and the ice physical temperature. Sea-ice dielectric properties also change significantly when ice transforms with time from FY into desalinated MY ice, with the latter producing decreased microwave attenuation, compared to the FY case. Fig. 2 illustrates the spatial distribution of FY and MY ice in the Arctic in October 2020 and March 2021 obtained from the Sea Ice Type product of the Ocean and Sea Ice Processing Center of European Meteorological Satellite (EUMETSAT) [29] (which is also reported in the SMOS-CS2 product), as well as the fractional areal coverage of each ice type over this time period. Due to their extensive coverage, both the FY and MY ice types should be considered in retrieval performance studies.

Empirical formulas for the sea-ice relative permittivity are frequently expressed in terms of the relative brine volume in the ice, υ, which is further expressed as a function of the ice salinity and physical temperature [30]

$$\upsilon = S\left(\frac{49.185}{\theta} + 0.532\right) \tag{1}$$

where S is the ice salinity (psu) and θ is the absolute value of the ice temperature in °C. Although both ice salinity and temperature can vary with depth within the sea-ice medium, a single "effective" value is frequently applied when the ice is described as a single layer. This approach is used in what follows, and the ice temperature and salinity values described can be considered to be effective values similar to

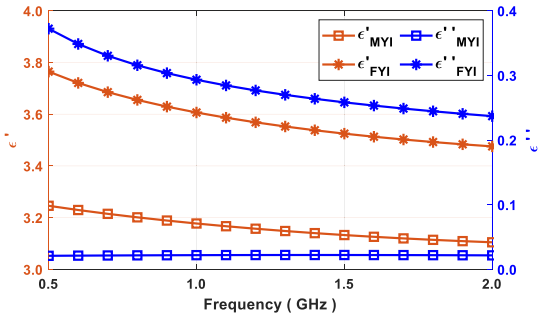

Fig. 3. Sea-ice relative permittivity from 0.5 to 2 GHz for FY ice (7 psu, −7 °C; stars) and MY ice (0.7 psu, −7 °C; squares).

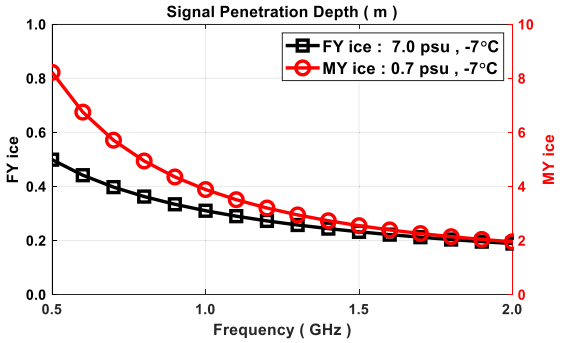

Fig. 4. Signal penetration depths for the specified sea-ice characteristics.

the mean values within the ice. Given v, the sea-ice relative permittivity ϵ can then be described as [31]

$$\epsilon = a_0 + a_1 v + j(b_0 + b_1 v) \tag{2}$$

where a_0, a_1, b_0, and b_1 are frequency-dependent coefficients that are distinct for the FY and MY ice types. Because these coefficients in [31] are provided for a limited number of frequencies, polynomial interpolations of the reported coefficients were applied to obtain a model for the 0.5–2-GHz range. Example relative permittivities as a function of ice type and frequency are illustrated in Fig. 3. Note the decrease in both the real and imaginary parts of the permittivity with frequency for both ice types and the greater imaginary part for FY ice. For the same cases, Fig. 4 plots the resulting penetration depths (at which the signal powers decline by ∼63%) for the assumption of semi-infinite sea-ice layers and shows ∼20- to ∼50-cm levels in the FY ice case that extends up to ∼2 to ∼8 m for MY ice and is greater in both cases at lower frequencies. The greater penetration depths obtained at lower frequencies even in the FY ice case again suggest that the inclusion of lower frequency measurements should improve the ability to retrieve ice properties for thicker ice. Beyond the examples shown, penetration depths typically decrease when either the ice salinity or temperature is increased due to the resulting increase in brine volume.

In what follows, sea water is assumed to have temperature and salinity values of −1.8 °C and 31 psu, respectively, which are reasonable characteristics for the Arctic. The sea water relative permittivity is obtained using [32] and remains fixed for all simulations. Snow layer dielectric properties

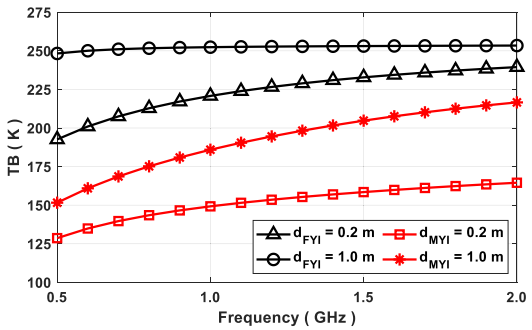

Fig. 5. Modeled TB from 0.5 to 2 GHz for FY ice with 7 psu, −7 °C, and MY ice with 0.7 psu, −7 °C. The snow depth, temperature, and density are 10 cm, −15 °C, and 0.35 g/cm^3, respectively.

are obtained using the mixing formula of [33] under the assumption of the dry snow expected prior to the onset of the melt season in the Arctic. The snow layer is described in terms of its density, temperature, and thickness.

B. Sea-Ice Emission Model

An incoherent radiative transfer (RT) model [34], [35] is used to compute the circularly polarized TB of the ice medium that would be measured by a nadir-observing radiometer. Circular polarization is considered in particular due to its desirable property of reducing the impacts of ionosphere-induced Faraday rotation for a space-borne system. The model includes the contributions of both up- and down-welling radiation and accounts for multiple reflections within the planar layered medium neglecting roughness on the ice and snow surfaces [36]. Coherent interactions are also neglected because it is assumed that ice roughness and thickness variations within a footprint of a satellite-borne radiometer antenna at low microwave frequencies are sufficient to extinguish any interference effects. Ice salinity, ice temperature, and snow density are assumed to be the constant effective values representing the respective layers. The model also treats sea ice and snow as homogeneous media so that volume scattering effects are neglected. This assumption is supported by the fact that snow grains, air bubbles, and brine pockets are much smaller than the electromagnetic wavelength from 0.5 to 2 GHz [37]. Reflections of both cosmic background radiation and atmospheric emissions (assumed ∼5 K) are also included. In Fig. 5, the described emission model was used to compare the frequency-dependent TB of a snow-covered sea-ice layer overlying sea water for both FY and MY ice of 20 or 100 cm thickness. Note that the TB increases with frequency in both cases, and the FY ice TB is larger than that for MY ice due to the high transmissivity obtained in the MY ice case.

The effect of a 15-cm thickness snow layer of varying snow density is examined in Fig. 6 for an example FY ice case. The presence of the snow layer is shown to increase the TB significantly by acting as an impedance matching layer at the ice/air interface. Fig. 6 shows the TB to be weakly sensitive to snow density for snow densities in the range of 0.25–0.5 g/cm^3; similar results are obtained as a function of both snow physical temperature and snow depth (not shown in Fig. 6). Due to the weak dependence of predicted TB on these snow

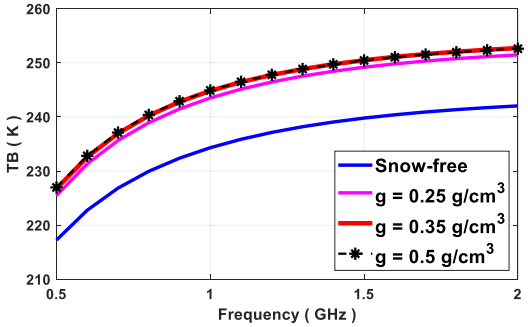

Fig. 6. Simulated TB for snow-covered FY ice of 0.5 m thickness, 7 psu, and −7 °C. The snow depth is 15 cm with an average temperature of −15 °C.

TABLE I
LUT CHARACTERISTICS USED IN THE SEA-ICE THICKNESS/SALINITY RETRIEVAL SIMULATIONS

Ice Thickness (m)			Ice Temperature (°C)		
Min.	*Max.*	*Res.*	*Min.*	*Max.*	*Res.*
0.01	3.00	0.01	-18.0	-3.0	0.1
FY Ice Salinity (psu)			**MY Ice Salinity (psu)**		
Min.	*Max.*	*Res.*	*Min.*	*Max.*	*Res.*
3.0	18.0	0.1	0.01	3.00	0.02

properties, the retrieval simulations that follow always include a snow layer having temperature, thickness, and density of −15 °C, 15 cm, and 0.35 g/cm^3, respectively, unless otherwise specified. It is noted that, while the electromagnetic effect of the snow layer itself is moderate, snow layers can have a greater impact on the ice temperature by insulating the ice from surrounding air temperatures. It is assumed in the retrieval simulations performed that a thermodynamic model is available, which accounts for these effects when providing ancillary information on the ice temperatures used in the forward model and retrieval process.

Using the forward model, TB lookup tables (LUT) were then generated as a function of ice thickness, ice salinity, ice temperature, and frequency for both FY and MY ice types using the parameter ranges specified in Table I. Note the differing salinity ranges used in the FY and MY cases. The salinity of newly formed FY ice (<10 cm) can exceed even the 18-psu upper limit of the LUT [38]; however, these extreme conditions are not analyzed in this study. The ice thickness upper bound is selected as 3 m, and the LUT resolution in thickness is 1 cm. Because a single ice layer is used in the model, the ice temperatures and salinities in the LUT can be considered effective values representing the impact of the true vertical profiles within the ice layer. The values used in Table I provide a sufficient resolution of salinity, thickness, and temperature for the retrieval performance simulations of interest in this article.

III. RETRIEVAL SIMULATIONS

Because the sea-ice emission model predicts that multiple combinations of input parameters can result in similar TB values, a direct inversion approach is not suitable for this problem. Instead, the sea-ice thickness (and also salinity for the TS retrieval) that minimizes the error between simulated measured TB and the forward model LUT is selected as the retrieved value. Ancillary input data are used to help resolve forward model ambiguities in this process; uncertainties in this ancillary sea-ice parameter information must also be incorporated in an analysis of retrieval errors. A Monte Carlo simulation process is used to characterize the error statistics obtained under differing conditions. The Monte Carlo simulation assumes that a wideband microwave radiometer provides TB measurements of the ice medium observed in up to 16 frequency channels 0.5, 0.6, …, 2 GHz. The simulated measurements are represented as the "truth" value from the LUT for a given condition corrupted by zero-mean Gaussian random noise of standard deviation σ_{NEDT} (K) that is independent in each frequency channel. Error statistics are computed using 1000 Monte Carlo trials for each case examined.

A. Retrieval Algorithm

The retrieval algorithm examines the difference between observed brightness temperatures $\text{TB}_{\text{test}}(f)$ as a function of $f = 1$ to up to 16 frequency channels and the LUT TB $\text{TB}_{\text{LUT}}(f, d, S, T)$ that depends on ice thickness d, salinity S, and temperature T. The root mean square error (RMSE), ξ, between the modeled and measured TB can be computed as

$$\xi(d, S, T) = \sqrt{\frac{1}{N}\sum_{f=1}^{N}(\text{TB}_{\text{test}}(f) - \text{TB}_{\text{LUT}}(f, d, S, T))^2}. \quad (3)$$

Due to the presence of significant ambiguities in the predicted TB across the thickness, salinity, and temperature spaces, the retrieval of all three parameters independently leads to significant errors. It is, therefore, desirable to include ancillary information to confine the retrieval space and increase retrieval accuracy. The TO and TS algorithms assume that ancillary information on ice salinity and temperature (TO) or ice temperature alone (TS), respectively, is available for use in the retrieval. The TO method then confines the retrieval space to a 1-D array of thicknesses (since ancillary salinity and temperature are provided), while the TS retrieval examines a 2-D matrix with dimensions of thickness and salinity (since only ancillary temperature is provided).

A brief summary of the TO retrieval algorithm is illustrated in Fig. 7. First, TB_{truth} is selected from the LUT given the specific thickness (d_o), salinity (S_o), and temperature (T_o) conditions of interest. A simulated observation TB_{test} is then created by adding zero-mean independent Gaussian random noise of standard deviation σ_{NEDT} to each frequency channel. The measured-model difference is then computed as a function of frequency and thickness as

$$\Delta(f, d) = \text{TB}_{\text{test}}(f) - \text{TB}_{\text{LUT}}(f, d, S_o, T_o) \quad (4)$$

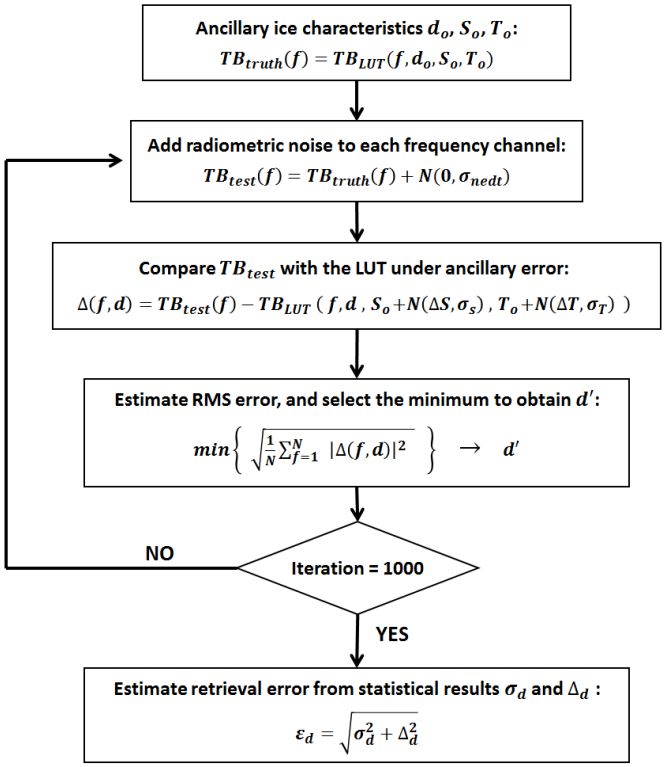

Fig. 7. Flowchart describing the steps of multichannel sea-ice retrieval simulation.

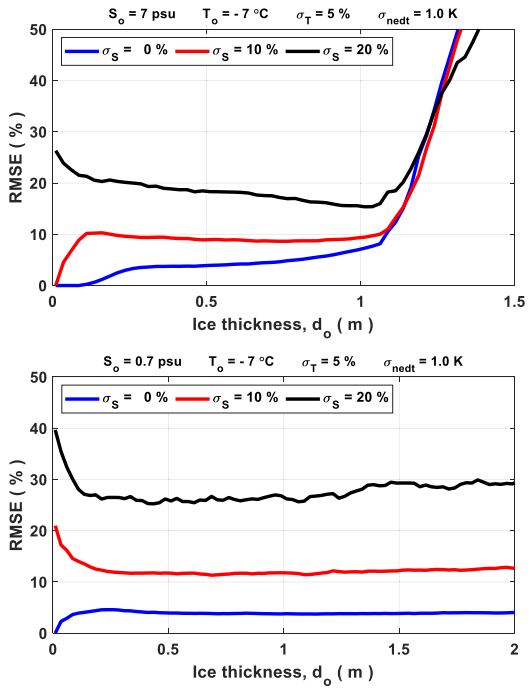

Fig. 8. Impact of ancillary salinity precision on thickness retrieval errors for (Top) FY and (Bottom) MY sea ice with characteristics specified in the plot titles.

where d denotes the thickness points in the LUT and f is the frequency channel, while S_o and T_o are the true sea-ice salinity and temperature, respectively, which, here, are assumed known from ancillary information (this represents the simplest case where no ancillary error is assumed). The retrieved thickness d' is then selected as that minimizes the RMSE from (3). After 1000 Monte Carlo trials, error statistics of d' compared to the truth value d_o are computed. The resulting thickness standard error ε_d can be expressed as

$$\varepsilon_d = \sqrt{\sigma_d^2 + \Delta_d^2} \tag{5}$$

where σ_d is the thickness standard deviation and Δ_d is the bias between d' and d_o. A similar approach is also used to estimate ice salinity errors for the TS retrieval case.

B. Modeling Errors in Ancillary Information

Both the TO and TS retrievals require ancillary information on sea-ice salinity and/or temperature. While ancillary information is available from meteorological models or other sources, it is unrealistic to assume that the information from such models is a perfect representation of truth conditions. To incorporate these uncertainties, errors in the ancillary information available were assumed for each Monte Carlo realization using

$$S_{\text{anc}} = S_o + N(\Delta S, \sigma_S) \tag{6}$$

$$T_{\text{anc}} = T_o + N(\Delta T, \sigma_T) \tag{7}$$

where S_{anc} and T_{anc} are the ancillary data used for a particular Monte Carlo realization that is obtained from the S_o and T_o truth values corrupted with normal random variables having mean values ΔS and ΔT and standard deviation σ_S and σ_T, respectively (see Fig. 7). The impact of these uncertainties on overall ice thickness and/or salinity retrievals can then be examined as a function of the mean and standard deviations of the errors introduced. Note that the impact of errors in the knowledge of ice concentration and inhomogeneities within the antenna footprint (e.g., ice thickness and roughness) is neglected in this initial study and will be considered in future work.

C. Retrieval Simulation Results

First, TO simulations were performed to investigate the effects of ancillary salinity and temperature precision, as shown in Figs. 8 and 9, respectively. In these simulations, all 16 frequency channels are used with $\sigma_{\text{NEDT}} = 1$ K for example ice temperature -7 °C and for example salinities 7 (FY) or 0.7 (MY) psu, and no bias in ancillary information is assumed (i.e., $\Delta S = \Delta T = 0$). Fig. 8 explores the impact of errors in ancillary salinity information as a function of ice thickness for FY (upper panel) and MY (lower) ice. In this simulation, the deviation in ancillary temperature σ_T is assumed to be 5% of the temperature ($\sim$0.35 °C). The results show that errors in ancillary salinity information have a significant impact on thickness retrieval performance (expressed in terms of percentage error in thickness) for both the FY and MY ice cases. In general, errors increase as the ancillary salinity precision degrades. For FY ice, errors remain largely independent of thickness until $\sim$1.1 m at which point sensitivity is lost. In the MY ice case, errors also depend only weakly on ice thickness up to 2 m. The modest reduction in error with thickness

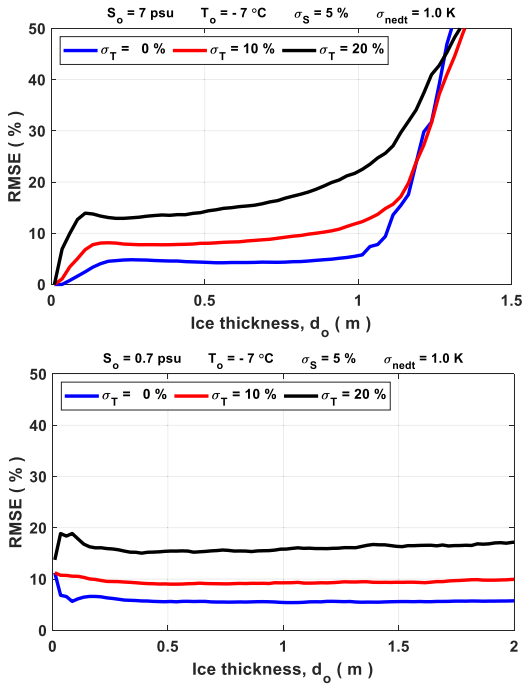

Fig. 9. Impact of ancillary temperature precision on thickness retrieval errors for (Top) FY and (Bottom) MY sea ice with characteristics specified in the plot titles.

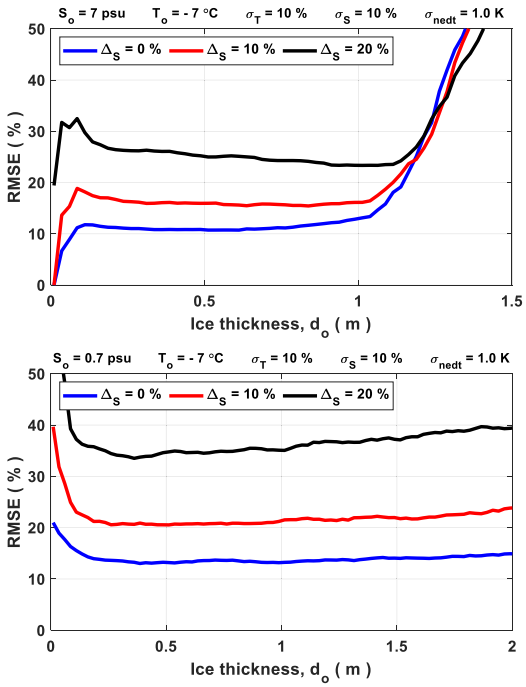

Fig. 10. Impact of ancillary salinity bias on thickness retrieval errors for (Top) FY and (Bottom) MY sea ice with characteristics specified in the plot titles.

observed for FY ice in the 20% salinity precision case likely results from the loss of sensitivity to salinity uncertainties as ice thicknesses increase.

Fig. 9 similarly explores the impact of temperature uncertainties for a fixed ancillary salinity deviation of 5% from the truth value (∼0.35 psu for FY ice and ∼0.035 psu for MY ice). Temperature uncertainties also have a significant impact on performance and show similar behaviors to those observed in Fig. 8 regarding both the FY and MY ice cases.

Figs. 10 and 11 further include biases in ancillary data for the same conditions, as in Figs. 8 and 9, and for σ_S and σ_T, both set to 10% of their respective truth values. When significant biases are added either to ice salinity (see Fig. 10) or temperature (see Fig. 11), retrieval errors increase due to mismatches between the true ice characteristics and the ancillary information. The error levels obtained can exceed 30% for larger biases and/or ancillary data standard deviations. Other simulations showed that negative ancillary biases yield slightly larger retrieval errors than positive biases; only the former is shown in the figures.

Fig. 12 examines thickness retrieval performance as a function of σ_{NEDT} for the case of no-bias in ancillary information, and for σ_S and σ_T, both set to 10% of their respective truth values. For the FY case, the results show that more precise TB measurements can decrease thickness retrieval errors for thicker ice. In contrast, changes in σ_{NEDT} have little impact on the MY ice case due to the high sensitivity to the thickness that is available in this case.

Fig. 13 compares thickness RMSE values for varying combinations of frequency channels used in the retrieval process for the same case, as shown in Fig. 12. The results show the importance of the lower frequency channels in the FY thick

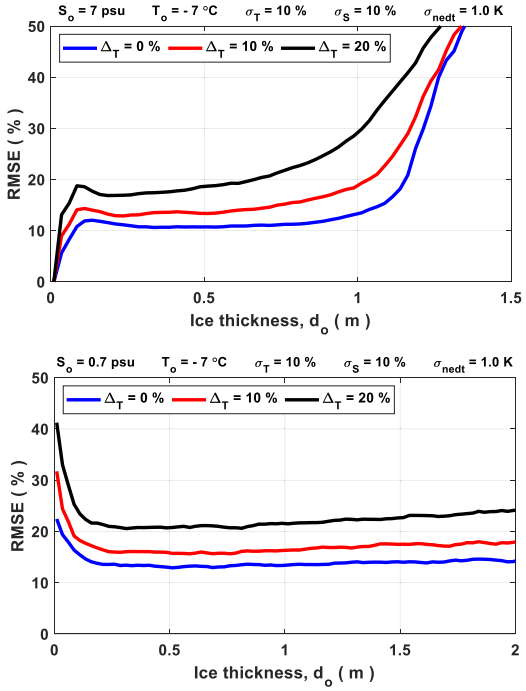

Fig. 11. Impact of ancillary temperature bias on thickness retrieval errors for (Top) FY and (Bottom) MY sea ice with characteristics specified in the plot titles.

ice case ($d_o > 30$ cm) due to their increased penetration depth, and the 16-channel retrieval has a performance similar to that of the lowest frequency channel alone. As expected, higher frequencies (1.4–2 GHz) alone show retrieval errors that increase rapidly when FY ice thicknesses exceed 20–30 cm. For MY ice, higher frequencies provide better performance since they are less sensitive to ice temperature uncertainties;

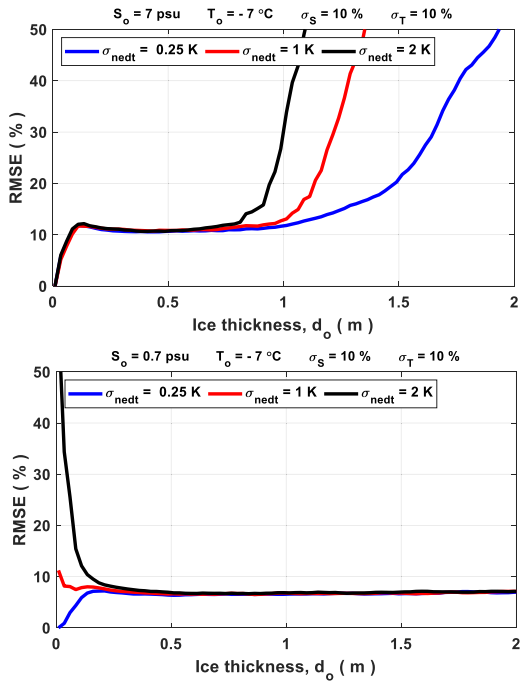

Fig. 12. Impact of radiometer noise on thickness retrieval errors for (Top) FY and (Bottom) MY sea ice with characteristics specified in the plot titles.

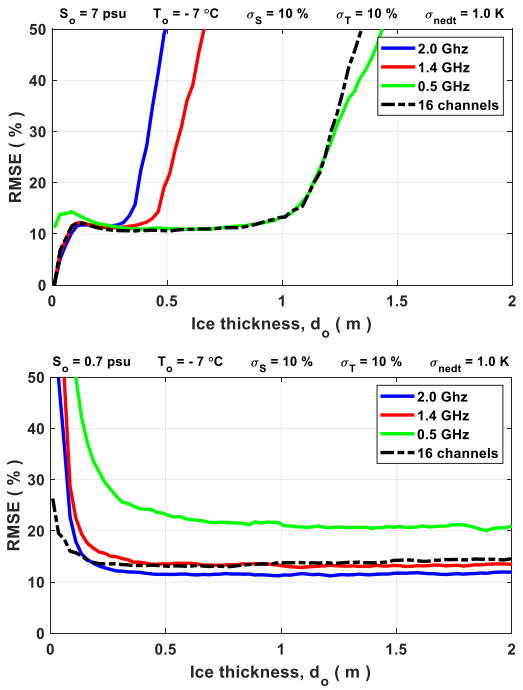

Fig. 13. Impact of frequency channels on thickness retrieval errors for (Top) FY and (Bottom) MY sea ice with characteristics specified in the plot titles.

the 16-channel retrieval performance is then similar to that of the highest frequency alone. Note these results are for a single case of ice temperature and salinity, and it should be expected that varying combinations of frequency channels will improve performance in other cases.

For the TS retrieval, errors in both the retrieved thickness and salinity can be computed. Error plots for both thickness and salinity versus sea-ice thickness are shown in Fig. 14 for the ice characteristics considered in Figs. 12 and 13 and for 16 frequency channels with $\sigma_{\mathrm{NEDT}} = 0.25$ K. Both retrieval errors vary significantly in the FY and MY ice cases, and are impacted by the ancillary temperature precision. The thickness precision is also degraded moderately compared to the TO approach due to the need to simultaneously estimate ice salinity. As in the TO case, FY ice thickness errors increase for thicker ice; this trend, however, is not observed for salinity errors. For MY ice, relative salinity errors tend to be larger than those for thickness due to the greater sensitivity of TB to salinity for MY ice. Fig. 15 considers an identical case but introduces an ancillary temperature bias while keeping the ancillary temperature precision at 5%. Larger biases in temperature clearly impact the results so that accurate ancillary temperature information is important in the TS retrieval.

The impact of radiometer noise on TS retrievals is illustrated in Fig. 16 for cases having no ancillary temperature bias but a 5% ancillary temperature precision. Performance is observed to vary significantly, with $\sigma_{\mathrm{NEDT}} < 1$ K appearing desirable. Finally, Fig. 17 illustrates the TS algorithm retrieval errors for varying combinations of frequency channels. Here, channel numbers 1, 4, and 16 refer to 0.5, 0.8, and 2.0 GHz, respectively, and the results are examined for channel 1 only, channels 1–4 only, or all 16 channels of the wideband radiometer. The single-channel option returns inaccurate results since the

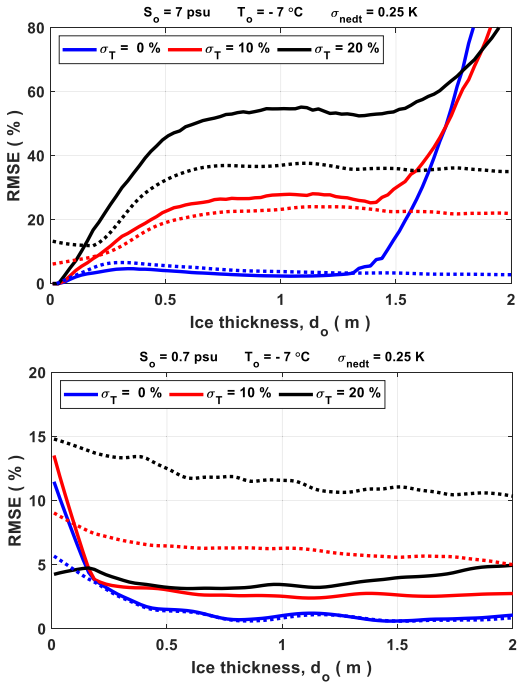

Fig. 14. Impact of ancillary temperature precision on thickness (solid curves) and salinity (dashed curves) TS retrieval for (Top) FY and (Bottom) MY sea ice with characteristics specified in the plot titles.

TS algorithm in this case attempts to infer two parameters from a single measurement. Adding frequency channels improves results for both FY and MY ice.

IV. Arctic-Scale Simulation

The results of Section III provided examples of the impact of ancillary data errors and instrument noise on retrieval

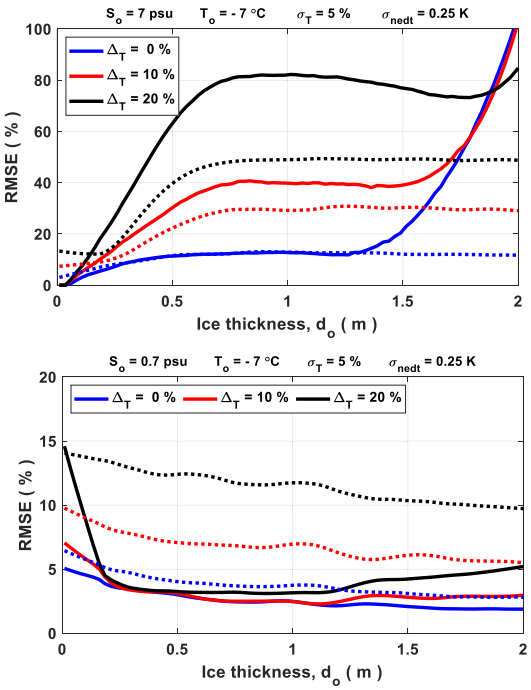

Fig. 15. Impact of ancillary temperature bias on thickness (solid curves) and salinity (dashed curves) TS method retrieval errors for (Top) FY and (Bottom) MY sea ice with characteristics specified in the plot titles.

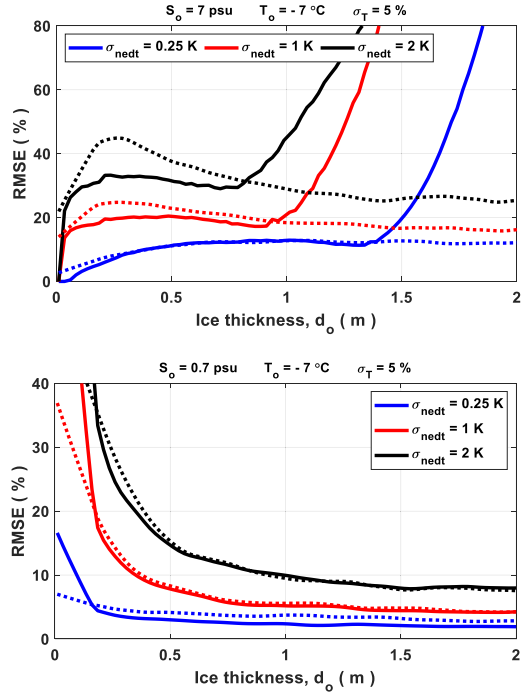

Fig. 16. Impact of radiometer noise on TS retrieval errors for (Top) FY and (Bottom) MY sea ice with characteristics specified in the plot titles. Solid and dashed curves represent thickness and salinity retrieval errors, respectively.

performance for specific "truth" sea-ice parameters. To obtain insight into retrieval performance averaged over "truth" parameters more representative of Arctic conditions, simulations were conducted for Arctic-scale thickness, salinity, and temperature conditions.

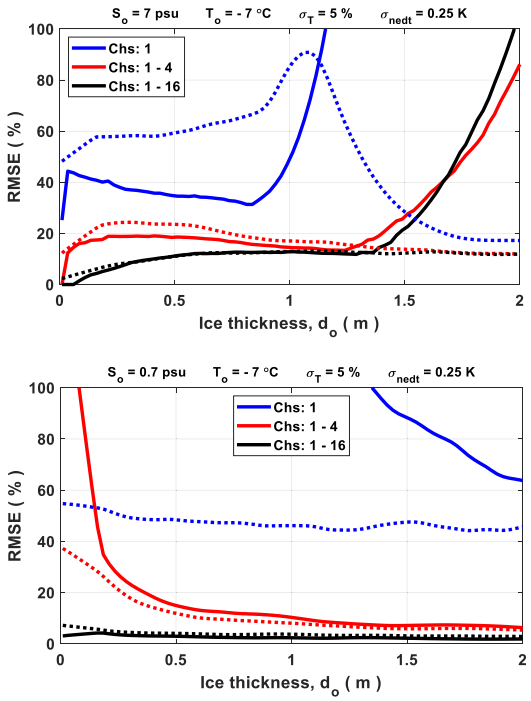

Fig. 17. Impact of frequency channels on TS retrieval errors for (Top) FY and (Bottom) MY sea ice with characteristics specified in the plot titles. Retrieval performance with single channel (0.5 GHz), four channels (0.5 through 0.8 GHz), or 16 channels (0.5 through 2.0 GHz) are demonstrated. Solid and dashed curves represent thickness and salinity retrieval errors, respectively.

The "truth" sea-ice types (i.e., FY or MY) and thicknesses were obtained from the Ocean and Sea Ice Satellite Application Facility (OSI-SAF) Sea Ice Type [29] and SMOS-CS2 datasets [18], respectively, from October 2020 to March 2021. The ice of thickness greater than 5 cm is further assumed to have an overlying snow layer of snow density of 0.35 g/cm^3 whose thickness is 10% that of the ice.

The "truth" sea-ice salinity (psu) was determined as a function of ice thickness through the semiempirical equations of [39]

$$S_{\mathrm{FYI}} = 14.24 - 19.39 * d, \quad d \leq 0.4 \text{ m} \tag{8}$$

$$S_{\mathrm{FYI}} = 7.88 - 1.59 * d, \quad d > 0.4 \text{ m} \tag{9}$$

$$S_{\mathrm{MYI}} = 1.58 + 0.18 * d \tag{10}$$

where d is the sea-ice thickness, and S_{FYI} and S_{MYI} are the FY and MY ice salinity, respectively. The truth salinities from (8) to (10) were further modified at each location by adding a zero mean, unit variance (in psu) normal random variate to model geophysical variability.

Truth air and ocean temperatures were obtained from the ERA-5 Reanalysis [40] from the same time period. The air and ocean temperatures were then used to estimate the sea-ice and snow "truth" temperatures following the steady-state thermodynamic model of [14].

Simulated observed TB corresponding to these conditions was then computed, and retrieval simulations are performed, as in Section III, which included both instrument measurement and ancillary data errors. Ancillary salinity information is determined in TO retrievals using the TS relations (8) through (10) as part of the retrieval process [without knowledge of the random variates perturbing the

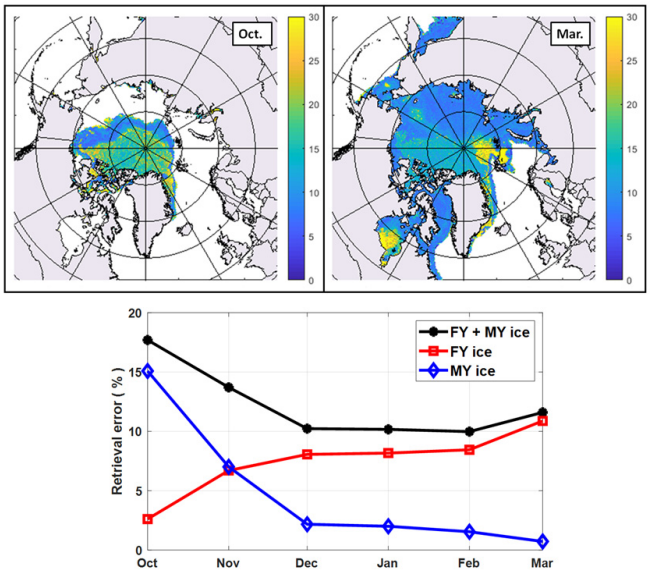

Fig. 18. Percent thickness error for TO retrievals in (Top) Arctic in October 2020 and March 2021 and (Bottom) monthly integrated error trends. The datapoints correspond to results from the first day of each month.

"truth" salinity from that calculated by (8)–(10)]. In addition, ancillary sea-ice temperature information in the retrieval is predicted through an empirical scaling of air temperatures

$$T_{\text{ice}} = c_1 * T_{\text{air}} + c_2 \tag{11}$$

in which the coefficients c_1 and c_2 were empirically determined ($c_1 = 0.278, c_2 = 195.3$ K) by comparing the modeled "truth" ice temperatures from [14] with the air temperature data from [40]. Note that this process introduces ancillary temperature biases as the ancillary ice temperatures are modeled using (11) at every location in the Arctic regardless of the ice and snow characteristics there.

Simulated TO retrieval errors in October 2020 and March 2021 are illustrated as a function of space in the top panel of Fig. 18 for 16 channels with $\sigma_{\text{NEDT}} = 0.25$ K, $\sigma_T = 0.3$ °C, and $\sigma_S = 0.6$ and 0.1 psu for FY and MY ice salinity, respectively. The results show thickness retrieval errors typically in the 5%–20% range that varies with the region considered.

The lower figure Fig. 18 presents monthly errors averaged over all retrievals and shows average errors that decrease as the winter progresses. The decrease observed results from the declining area occupied by MY ice since errors for this ice type are more sensitive to ancillary errors in ice salinity. Errors rise again in March when the areal coverage of thicker FY ice increases.

Similar results for the same assumptions are shown in Fig. 19 for the TS approach with relative errors in thickness and salinity shown in the top and middle plots, respectively, and monthly averages in the lower plot. Errors are larger than in the TO case but remain in the 10%–20% level for both thickness and salinity with an increasing trend over the winter due to the increase in FY ice coverage. The increased TO retrieval errors in October are not observed in this case since the salinity is also determined by the algorithm.

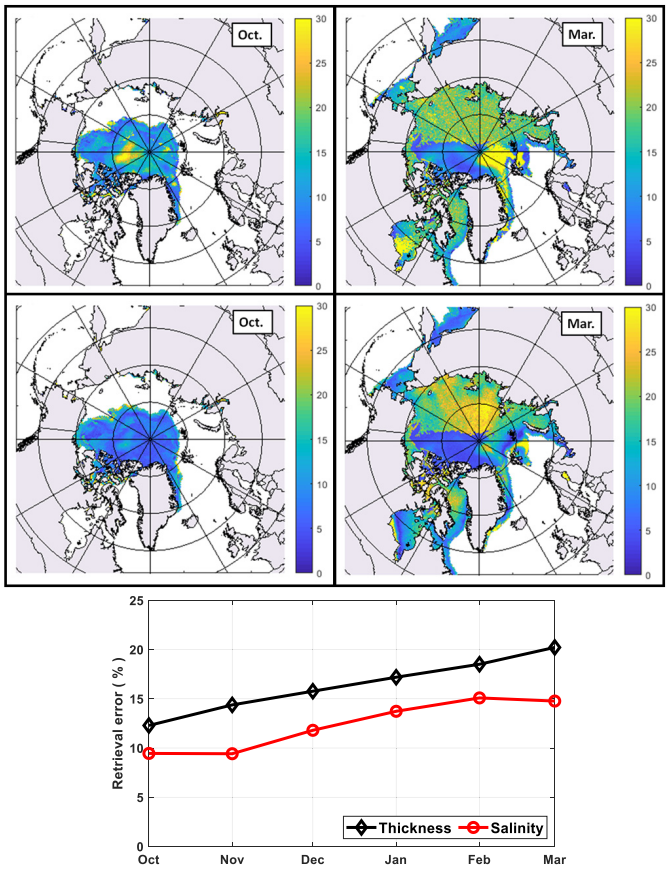

Fig. 19. TS retrieval error distributions in (Top) Arctic in October and March for thickness, (Middle) salinity, and (Bottom) monthly integrated error trend for each sea-ice parameter. The datapoints correspond to results from the first day of each month.

Although the spatial maps shown in Figs. 18 and 19 should be interpreted with caution since potential ice inhomogeneities and ice concentration effects are not included, the spatial distributions shown nevertheless provide potentially useful performance insights. For example, MY ice regions in the north of Canada and Greenland show relatively low thickness errors with the TS retrieval in March (see Fig. 19) whereas degraded performance is observed in the same region with the TO retrieval (see Fig. 18). This can be attributed both to the characteristics of MY ice and the retrieval method used. In particular, the TO retrieval requires ancillary salinity data, and MY ice retrievals are highly sensitive to ancillary salinity biases (see Fig. 10). Therefore, inaccurate salinity assumptions can lead to poor performance. The TS retrieval on the other hand does not use ancillary salinity information, eliminating this source of error. High thickness retrieval errors also occur to the north of Svalbard and in Hudson Bay. As shown in Fig. 20, these FY ice regions have larger thicknesses and higher air temperatures so that the increased errors are likely associated with the impact of errors in ancillary ice temperature information. In particular, (11) estimates different ice temperatures in these regions compared to the true values calculated from thermodynamic modeling. This effect is not observed in nearby thin FY ice regions due to the reduced sensitivity to ancillary temperature errors in this case.

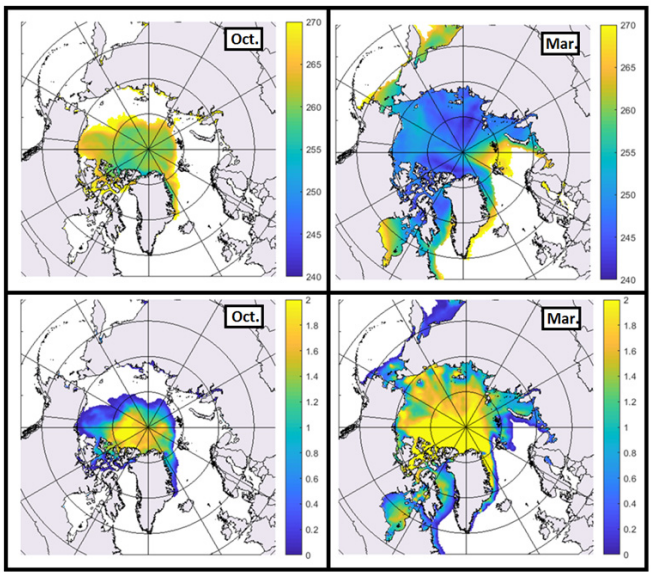

Fig. 20. Air temperature [40] (Top, in K) and ice thickness [18] (Bottom, in meters) distributions in the Arctic in October and March. The distributions are from the first day of each month.

V. Discussion and Conclusion

The simulations performed demonstrate the potential performance of a multichannel wideband radiometer in retrieving sea-ice thickness and salinity under various conditions. The retrieval errors obtained depend on the ice type (FY/MY), retrieval approach (TO/TS), frequency channels used, measurement noise, and errors in ancillary information. The results generally confirm that the use of frequencies below 1.4 GHz improves sensitivity to sea-ice thickness beyond that available from current L-band radiometers. The joint retrieval of ice thickness and salinity also is feasible when multiple frequency channels are used. TO retrievals provide lower ice thickness retrieval errors and can even in some cases obtain reasonable performance with a single low-frequency channel (e.g., 0.5 GHz). However, the requirement for ancillary information on both ice salinity and temperature is a challenge that particularly impacts thickness retrievals for low salinity MY ice since TB is highly sensitive to ice salinity in this case. The joint temperature/salinity (TS) retrieval instead requires ancillary information only on ice temperature information and, thereby, avoids the impact of errors in ancillary salinity data. This method, however, requires the use of multiple frequency channels, and the performance is highly dependent on the level of measurement noise.

The simulation of retrieval errors over the entire Arctic generally showed that both the TO and TS approaches can yield relative thickness errors in the 5%–20% range, and the TO approach typically yields improved thickness retrievals compared to the TS approach for the parameters considered.

It is noted that the simulations reported do not take into account inhomogeneities in ice and snow characteristics within a footprint (including ice concentration) and multilayered sea ice; the impact of these inhomogeneities should be expected to increase as the observed footprint becomes larger. Future work will explore these effects. The results shown in the article should, therefore, be considered a "best case" scenario. Despite this limitation, the results reported further demonstrate the potential of 0.5–2-GHz microwave radiometry for advancing the remote sensing of sea-ice properties and the Earth's environment more generally [41], [42].

Acknowledgment

The production of the merged CryoSat-SMOS sea-ice thickness data was funded by the European Space Agency (ESA) Project SMOS and CryoSat-2 Sea Ice Data Product Processing and Dissemination Service, and data from October 2020 to March 2021 were obtained from Alfred Wegener Institute (AWI). H. Hersbach *et al.*, (2018) was downloaded from the Copernicus Climate Change Service (C3S) Climate Data Store. The results contain modified C3S information 2021. Neither the European Commission nor the European Center for Medium-Range Weather Forecasts (ECMWF) is responsible for any use that may be made of the Copernicus information or data it contains. The scientific results and conclusions, as well as any views or opinions expressed herein, are those of the authors and do not necessarily reflect those of the National Oceanic and Atmospheric Administration (NOAA) or the U.S. Department of Commerce. The Institute of Applied Physics Nello Carrara (IFAC) activity was partially supported by the Italian Space Agency (ASI) Project Cryorad Follow-On under Contract 2021-1-U.0.

References

[1] M. Meredith *et al.*, "Polar regions," IPCC Special Rep. Ocean Cryosphere Changing Climate, IPCC, WMO, UNEP, Intergovernmental Panel Climate Change (IPCC), Geneva, Switzerland, Tech. Rep. IPCC, 2019, pp. 203–320. [Online]. Available: https://www.ipcc.ch/srocc/home/

[2] R. Lindsay and A. Schweiger, "Arctic sea ice thickness loss determined using subsurface, aircraft, and satellite observations," *Cryosphere*, vol. 9, no. 1, pp. 269–283, Feb. 2015, doi: 10.5194/tc-9-269-2015.

[3] P. Gloersen, W. J. Campbell, D. J. Cavalieri, J. C. Comiso, C. L. Parkinson, and H. J. Zwally, "Satellite passive microwave observations and analysis of Arctic and Antarctic sea ice 1978–1987," *Ann. Glaciol.*, vol. 17, pp. 149-154, 1992.

[4] D. J. Cavalieri, C. L. Parkinson, P. Gloersen, and H. J. Zwally, "Sea ice concentrations from Nimbus-7 SMMR and DMSP SSM/I-SSMIS passive microwave data, version 1. (Updated yearly)," NASA Nat. Snow Ice Data Center Distrib., Act. Arch., Boulder, CO, USA, Tech. Rep., 1996, doi: 10.5067/8GQ8LZQVL0VL.

[5] N. Zakhvatkina, V. Smirnov, and I. Bychkova, "Satellite SAR data-based sea ice classification: An overview," *Geosciences*, vol. 9, no. 4, p. 152, Mar. 2019.

[6] R. Kwok, J. C. Curlander, R. McConnell, and S. S. Pang, "An ice-motion tracking system at the Alaska SAR facility," *IEEE J. Ocean. Eng.*, vol. 15, no. 1, pp. 44–54, Jan. 1990, doi: 10.1109/48.46835.

[7] T. Lavergne, S. Eastwood, Z. Teffah, H. Schyberg, and L. -A. Breivik, "Sea ice motion from low-resolution satellite sensors: An alternative method and its validation in the Arctic," *J. Geophys. Res., Oceans*, vol. 115, no. C10, pp. 1–14, Oct. 2010, doi: 10.1029/2009JC005958.

[8] M. Mäkynen, B. Cheng, and M. Similä, "On the accuracy of thin-ice thickness retrieval using MODIS thermal imagery over Arctic first-year ice," *Ann. Glaciol.*, vol. 54, no. 62, pp. 87–96, 2013, doi: 10.3189/2013AoG62A166.

[9] Y. Yu and D. A. Rothrock, "Thin ice thickness from satellite thermal imagery," *J. Geophys. Res.*, vol. 101, no. C11, pp. 25753–25766, Nov. 1996, doi: 10.1002/2013RG000431.

[10] X. Wang, J. R. Key, and Y. Liu, "A thermodynamic model for estimating sea and lake ice thickness with optical satellite data," *J. Geophys. Res.*, vol. 115, no. C12, pp. 1–14, 2010, doi: 10.1029/2009JC005857.

[11] G. A. Maykut and N. Untersteiner, "Some results from a time-dependent thermodynamic model of sea ice," *J. Geophys. Res.*, vol. 76, no. 6, pp. 1550–1575, Feb. 1971, doi: 10.1029/JC076i006p01550.

[12] R. Kwok and G. F. Cunningham, "Variability of Arctic sea ice thickness and volume from CryoSat-2," *Phil. Trans. Roy. Soc. A, Math., Phys. Eng. Sci.*, vol. 373, no. 2045, Jul. 2015, Art. no. 20140157, doi: 10.1098/rsta.2014.0157.
[13] S. W. Laxon *et al.*, "CryoSat-2 estimates of Arctic sea ice thickness and volume," *Geophys. Res. Lett.*, vol. 40, no. 4, pp. 732–737, Feb. 2013, doi: 10.1002/grl.50193.
[14] X. Tian-Kunze *et al.*, "SMOS-derived thin sea ice thickness: Algorithm baseline, product specifications and initial verification," *Cryosphere*, vol. 8, no. 3, pp. 997–1018, 2014.
[15] L. Kaleschke, N. Maaß, C. Haas, S. Hendricks, G. Heygster, and R. Tonboe, "A sea-ice thickness retrieval model for 1.4 GHz radiometry and application to airborne measurements over low salinity sea-ice," *Cryosphere*, vol. 4, no. 4, pp. 583–592, 2010, doi: 10.5194/tc-4-583-2010.
[16] C. Paţilea, G. Heygster, M. Huntemann, and G. Spreen, "Combined SMAP–SMOS thin sea ice thickness retrieval," *Cryosphere*, vol. 13, no. 2, pp. 675–691, Feb. 2019.
[17] A. Schmitt and L. Kaleschke, "A consistent combination of brightness temperatures from SMOS and SMAP over polar oceans for sea ice applications," *Remote Sens.*, vol. 10, no. 4, p. 553, Apr. 2018, doi: 10.3390/rs10040553.
[18] R. Ricker, S. Hendricks, L. Kaleschke, X. Tian-Kunze, J. King, and C. Haas, "A weekly Arctic sea-ice thickness data record from merged CryoSat-2 and SMOS satellite data," *Cryosphere*, vol. 11, pp. 1607–1623, Jul. 2017, doi: 10.5194/tc-11-1607-2017.
[19] M. T. Hallikainen, "A new low-salinity sea-ice model for UHF radiometry," *Int. J. Remote Sens.*, vol. 4, no. 3, pp. 655–681, 1983, doi: 10.1080/01431168308948581.
[20] K. C. Jezek *et al.*, "500–2000-MHz brightness temperature spectra of the northwestern Greenland ice sheet," *IEEE Trans. Geosci. Remote Sens.*, vol. 56, no. 3, pp. 1485–1496, Mar. 2018, doi: 10.1109/TGRS.2017.2764381.
[21] M. Brogioni *et al.*, "500–2000-MHz airborne brightness temperature measurements over the east Antarctic plateau," *IEEE Geosci. Remote Sens. Lett.*, vol. 19, pp. 1–5, 2021.
[22] O. Demir *et al.*, "Measurements of 540–1740 MHz brightness temperatures of sea ice during the winter of the MOSAiC campaign," *IEEE Trans. Geosci. Remote Sens.*, vol. 60, pp. 1–11, 2022, doi: 10.1109/TGRS.2021.3105360.
[23] J. T. Johnson *et al.*, "The Ultra-wideband Software-Defined Radiometer (UWBRAD) for ice sheet internal temperature sensing: Results from recent observations," in *Proc. IGARSS*, Jul. 2016, pp. 7085–7087, doi: 10.1109/IGARSS.2016.7730848.
[24] M. J. Andrews *et al.*, "The ultrawideband software-defined microwave radiometer: Instrument description and initial campaign results," *IEEE Trans. Geosci. Remote Sens.*, vol. 56, no. 10, pp. 5923–5935, Oct. 2018.
[25] B. J. Peterson, J. McClelland, R. Curry, R. M. Holmes, J. E. Walsh, and K. Aagaard, "Trajectory shifts in the Arctic and subarctic freshwater cycle," *Science*, vol. 313, no. 5790, pp. 1061–1066, Aug. 2006, doi: 10.1126/science.1122593.
[26] F. A. Haumann *et al.*, "Supercooled southern ocean waters," *Geophys. Res. Lett.*, vol. 47, no. 20, Oct. 2020, doi: 10.1029/2020GL090242.
[27] M. Vancoppenolle, T. Fichefet, and H. Goosse, "Simulating the mass balance and salinity of Arctic and Antarctic sea ice. 2. Importance of sea ice salinity variations," *Ocean Model.*, vol. 27, nos. 1–2, pp. 54–69, Jan. 2009, doi: 10.1016/j.ocemod.2008.11.003.
[28] K. Jezek *et al.*, "Remote sensing of sea ice thickness and salinity with 0.5–2 GHz microwave radiometry," *IEEE Trans. Geosci. Remote Sens.*, vol. 57, no. 11, pp. 8672–8684, Jul. 2019.
[29] EUMETSAT Ocean and Sea ice Center. (2022). *Sea Ice Type (Product OSA-403-d)*. [Online]. Available: https://osisaf-hl.met.no/osi-402-403-d-desc
[30] G. Frankenstein and R. Garner, "Equations for determining the brine volume of sea ice from −0.5° to −22.9° C.," *J. Glaciol.*, vol. 6, no. 48, pp. 943–944, 1967.
[31] M. Vant, R. O. Ramseier, and V. Makios, "The complex-dielectric constant of sea ice at frequencies in the range 0.1–40 GHz," *J. Appl. Phys.*, vol. 49, no. 3, pp. 1264–1280, 1978.
[32] L. Klein and C. Swift, "An improved model for the dielectric constant of sea water at microwave frequencies," *IEEE J. Ocean. Eng.*, vol. OE-2, no. 1, pp. 104–111, Jan. 1976.
[33] A. Sihvola, E. Nyfors, and M. Tiuri, "Mixing formulae and experimental results for the dielectric constant of snow," *J. Glaciol.*, vol. 31, no. 108, pp. 163–170, 1985.
[34] F. Ulaby, R. Moore, and A. Fung, *Microwave Remote Sensing: Active and Passive*. Norwood, MA, USA: Artech House, 1981, p. 243.
[35] P. Mills and G. Heygster, "Sea ice emissivity modeling at L-band and application to 2007 pol-ice campaign field data," *IEEE Trans. Geosci. Remote Sens.*, vol. 49, no. 2, pp. 612–627, Feb. 2011.
[36] M. Miernecki, L. Kaleschke, N. Maaß, S. Hendricks, and S. S. Søbjærg, "Effects of decimetre-scale surface roughness on L-band brightness temperature of sea ice," *Cryosphere*, vol. 14, no. 2, pp. 461–476, Feb. 2020, doi: 10.5194/tc-14-461-2020.
[37] D. G. Barber *et al.*, "The role of snow on microwave emission and scattering over first-year sea ice," *IEEE Trans. Geosci. Remote Sens.*, vol. 36, no. 5, pp. 1750–1763, Sep. 1998.
[38] A. I. Ryvlin, "Method of forecasting flexural strength of an ice cover," *Problem Arct. Antarct.*, vol. 45, pp. 79–86, 1974.
[39] D. F. N. Cox and W. F. Weeks, "Salinity variations in sea ice," *J. Glaciol.*, vol. 13, no. 67, pp. 109–120, 1974.
[40] H. Hersbach *et al.* (2018). ERA5 hourly data on single levels from 1979 to present. Copernicus Climate Change Service (C3S) Climate Data Store (CDS). Accessed: Aug. 23, 2021, doi: 10.24381/cds.adbb2d47.
[41] J. T. Johnson *et al.*, "Microwave radiometry at frequencies from 500 to 1400 MHz: An emerging technology for Earth observations," *IEEE J. Sel. Topics Appl. Earth Observ. Remote Sens.*, vol. 14, pp. 4894–4914, 2021, doi: 10.1109/JSTARS.2021.3073286.
[42] G. Macelloni *et al.*, "Cryorad: A low frequency wideband radiometer mission for the study of the cryosphere," in *Proc. IEEE Int. Geosci. Remote Sens. Symp. (IGARSS)*, Jul. 2018, pp. 1998–2000.

Oguz Demir received the B.Sc. and M.Sc. degrees in electrical and electronics engineering from Middle East Technical University, Ankara, Turkey, in 2013 and 2017, respectively. He is currently pursuing the Ph.D. degree with the Electroscience Laboratory, The Ohio State University, Columbus, OH, USA.

From 2013 to 2017, he was an RF/Microwave Engineer with Aselsan Inc., Ankara, where he was involved in designing microwave circuits for very high frequency (VHF)/UHF radios and 4G/Long-Term-Evolution (LTE) base stations. He is currently a Graduate Research Associate with the Electroscience Laboratory, The Ohio State University. As part of his studies, he participated in the MOSAiC Expedition in 2019 to operate an ultrawideband microwave radiometer to measure sea-ice thermal emissions. His research interests include microwave remote sensing and ultra-wideband radiometry for sea-ice observations.

Joel T. Johnson (Fellow, IEEE) received the B.E.E. degree from the Georgia Institute of Technology, Atlanta, GA, USA, in 1991, and the S.M. and Ph.D. degrees from the Massachusetts Institute of Technology, Cambridge, MA, USA, in 1993 and 1996, respectively.

He is currently a Burn and Sue Lin Professor with the Electroscience Laboratory, Department of Electrical and Computer Engineering, The Ohio State University, Columbus, OH, USA. His research interests are in the areas of microwave remote sensing, propagation, and electromagnetic wave theory.

Dr. Johnson is a member of Commissions B and F of the International Union of Radio Science (URSI), and a member of Tau Beta Pi, Eta Kappa Nu, and Phi Kappa Phi. He was a recipient of the 1993 Best Paper Award from the IEEE Geoscience and Remote Sensing Society, was named an Office of Naval Research Young Investigator, National Science Foundation Career Awardee, and the PECASE award recipient in 1997, and was recognized by the U.S. National Committee of URSI as a Booker Fellow in 2002.

Kenneth C. Jezek received the B.S. degree in physics from the University of Illinois at Urbana-Champaign, Champaign, IL, USA, in 1973, and the M.S. and Ph.D. degrees in geophysics from the University of Wisconsin–Madison, Madison, WI, USA, in 1977 and 1980, respectively, with focus on the behavior of the Ross Ice Shelf, Antarctica, using ice sounding radar data collected during several visits to the Antarctic.

He was the Manager of the NASA's Polar Oceans and Ice Sheets Program. He was a Geophysicist with the U.S. Army Cold Regions Research and Engineering Laboratory, Hanover, NH, USA, where he was involved in the electromagnetic and acoustical properties of sea ice in the laboratory and the Arctic. In 1989, he was the Director of the Byrd Polar Research Center, School of Earth Sciences, The Ohio State University (OSU), Columbus, OH, USA, where he is currently a Professor Emeritus. From 1997 to 2007, he led the Radarsat Antarctic Mapping Project. His research interests include the application of ultrawideband radiometry to the ice sheet and sea-ice studies. He served as a Co-Leader of the International Polar Year GIIPSY project that involved the participation of 12 space agencies from 2007 to 2010.

Dr. Jezek has been serving on 13 NRC committees since 1989. He Chaired the Land Ice Science Team for NASA's Operation Icebridge from 2010 to 2013.

Marco Brogioni (Member, IEEE) was born in Siena, Italy, in 1976. He received the M.Sc. degree in telecommunications engineering with the University of Siena, Siena, Italy, in 2003, and the Ph.D. degree in remote sensing from the University of Pisa, Pisa, Italy, in 2008.

Since 2004, he has been with the Microwave Remote Sensing Group, Institute of Applied Physics Nello Carrara (IFAC), Consiglio Nazionale delle Ricerche (CNR), Florence, Italy. From 2006 to 2007, he has been a Visiting Student with the University of California at Santa Barbara, Santa Barbara, CA, USA. He is currently involved in several international projects regarding polar regions. His research interests include passive and active microwave remote sensing applied to snow by using satellite and ground-based data, especially the development of electromagnetic models for passive and active microwave remote sensing of snow, vegetation, and soil. He is also involved in the design and manufacturing of microwave radiometers (P- to Ka-bands).

Dr. Brogioni was a recipient of the Third Prize at the URSI GA Student Prize Paper Competition in Chicago, IL, USA, in 2008. He served as the Chair of the 16th MicroRad 2020 virtual meeting and in the local organizing committee of the Tenth Microrad, Florence, in 2008 and the Microwave Signature Symposium of the URSI Commission-F, Florence, in 2010. He participated in the Italian Antarctic Expeditions, carrying out his research at Concordia Station (Dome-C) and Mario Zucchelli Station (Ross Sea) in 2013, 2015, and 2018.

Giovanni Macelloni (Senior Member, IEEE) received the M.Sc. degree in electronic engineering from the University of Florence, Florence, Italy, in 1993.

Since 1995, he has been with the Institute of Applied Physics-CNR, Florence, where he is currently a Senior Scientist. Since 2019, he has been an Adjunct Professor with the University of Venice, Venice, Italy. His research interest includes microwave active and passive remote sensing for the study of the Earth System and cryosphere in particular. He is also involved in the design and development of microwave remote sensing systems both from the ground, airborne, and satellite. The research is carried out in the framework of several national and international programs granted by Italian entities, the European Community, and space agencies (the European Space Agency (ESA), Paris, France, the Italian Space Agency (ASI), Rome, Italy, NASA, Washington, DC, USA, and JAXA, Tokyo, Japan) and includes the participation to international teams for the studying of the cryosphere and the development and assessment of future space-borne missions.

Mr. Macelloni is a member of the Cryonet team of Global Cryosphere Watch of the WMO and the Italian Scientific Antarctic Commission, which implements that the National Antarctic Program is the Italian National delegate at the Scientific Committee of Antarctic Research. He was a tutor of Ph.D. students, served as a reviewer of several international committees, organizations, and international journals, and acted as an organizer and the co-chair of international conferences. He is currently an Associate Editor of the IEEE TRANSACTIONS ON GEO-SCIENCE AND REMOTE SENSING.

Lars Kaleschke received the M.Sc. and Ph.D. degrees in physics from the University of Bremen, Bremen, Germany, in 1998 and 2003, respectively.

From 2006 to 2018, he served as a Professor with the Institute of Oceanography, Universität Hamburg, Hamburg, Germany, where he was involved in setting up the DFG Cluster of Excellence for climate research. There he headed the research topic Arctic Regions and Permafrost. He coordinated various research projects and was involved in developing and testing a system for ice prediction and route optimization to facilitate safe and efficient navigation for ships operating on the ice. In 2019, he moved to the Alfred Wegener Institute (AWI), Bremerhaven, Germany, and subsequently took part in the longest leg of MOSAiC, the largest expedition to the Central Arctic to date. The measurements that he took on the sea ice using microwave radiometers are essential for the further development and validation of satellite-based methods used for comprehensive observation of the polar regions. He is currently an expert on remote sensing with the Sea Ice Physics Section, Helmholtz Centre for Polar and Marine Research, AWI.

Ludovic Brucker received the M.S. degree in physics from the University of Clermont-Ferrand, Clermont-Ferrand, France, in 2006, and the Ph.D. degree in earth and environmental science from Grenoble Alpes University, Grenoble, France, in 2009.

He works with the Satellite Oceanography and Climatology Division, National Oceanic and Atmospheric Administration (NOAA)/NESDIS Center for Satellite Applications and Research (STAR), College Park, MD, USA, where he has been serving as the Chief Scientist with the U.S. National Ice Center, since 2021. Prior to this appointment, he has contributed to microwave remote sensing of the cryosphere with NASA Goddard Space Flight Center, Greenbelt, MD, USA, for 12 years. One of his primary roles is to identify novel remote sensing applications for the cryosphere and to enable their transition from research to operations for societal benefits. He has published more than 60 articles and participated in a dozen field campaigns, including polar deployments in Antarctica, Greenland, and the Canadian Archipelago.

Dr. Brucker was a co-recipient of the 2021 IEEE Geoscience and Remote Sensing Transactions Prize Paper Award.